



京都大学 防災研究所  
Disaster Prevention Research Institute  
Kyoto University

国際共同研究  
2022W-03

大規模地すべりの発生前兆現象の検出と災害軽減  
Detecting the precursor for the occurrence of large-scale  
landslides and disaster mitigation

May 28, 2024

Coordinator Yao JIANG

Final Report for  
the International Collaborative Research  
Disaster Prevention Research Institute, Kyoto University

**Project No.: 2022W-03**

To the Director of the Disaster Prevention Research Institute, Kyoto University,

Applicant (Principal Investigator)

Name : JIANG Yao

Position: Professor

Affiliation: Institute of Mountain Hazards and Environment, Chinese Academy of Sciences, China

**Project Title:**

Detecting the precursor for the occurrence of large-scale landslides and disaster mitigation

Principal Investigator : JIANG Yao

Affiliation : Institute of Mountain Hazards and Environment  
Chinese Academy of Sciences, China

Contact Person at DPRI: WANG Gonghui

Research Period : From April 1, 2022 to March 31, 2024

Research Location : Research Center for Landslide Disaster Risk Cognition and Reduction, DPRI, Kyoto University;  
Some giant landslides triggered by the 2008 Wenchuan earthquake in China; Nishiikawa  
landslide in Tokushima, Japan

Number of the Participants in the Project : 16 (DPRI: 4 / non-DPRI: 12 )

**Anticipated Impact on Research and Education:**

Seven graduate students participated in this project, three of them from the graduate school of science, Kyoto University, and two from Toyama Prefectural University, and two from Institute of Mountain Hazards and Environment, Chinese Academy of Sciences, China. Through involving this project, the students elevated their knowledge of the landslide movement mechanisms, landsliding monitoring, and geophysical issues in landslide study. The results make a significant contribution to landslide science and may help us better the forecast of landslides.

## **Research Report**

### **1. Purpose**

In recent years, disastrous landslides occurred at many regions over the world, such as the 2011 large-scale landslides in the Kii Mountains, Japan, the 2013 Izu-Oshima debris avalanche in Japan, the 2014 Oso landslide in USA, and the 2014 Hiroshima landslides in Japan. All of them caused great loss of casualties and damage. To prevent or at least to mitigate this kind of landslide disaster, it will be of great importance to understand the initiation and development processes, especially to detect the precursory phenomena for proper early warning and evacuation.

The main purpose of this study is to detect and quantify the precursory phenomena associated with the initial stages for large-scale landslides. This will be achieved by advancing a series of shear tests in the laboratory to identify different parameters affecting the generation of acoustic waveforms (AEs), complementing with developing a viable monitoring system to record the precursory phenomena on the field of a large landslide in Japan. By performing the combined analysis of the experimental and field datasets, the ultimate purpose of this study is to reveal the pre-failure mechanisms for large-scale landslides and then to provide a more appropriate way for mitigating the related landslide disaster.

### **2 Summary of research progress**

To detect the precursors for the occurrence of landslides and then provide information for the landslide disaster mitigation, as the first phase, we conducted a series of direct shear-AE tests to investigate the relationship between characteristics of AE and mechanical behavior of granular in stick-slip events. We used spherical glass beads (1.0–3.0 mm in diameter) to represent particles. Shearing was performed in a strain-controlled way at a constant shear speed of 0.1, 0.4, 0.8 or 1.2 mm/min and constant normal stress of 50, 100, 200 or 300 kPa. In order to detect the energy released inside the samples, three equally spaced acoustic emission (AE) transducers were installed around the shear box. Additionally, using the external parameter interface of the AE system, we collected the AE waveform, shear stress and displacement at the same time, which allowed us to accurately explore the relationship between characteristics of AE and mechanical behavior in the shear process. To examine the shear behaviors of granular materials from the point of view of shear energy, we also conducted ring shear tests on different types of soil samples and examined their shear behavior by changing the shear rates and observing the formation of shear zones.

As the second phase of this study, we installed AE monitoring system in a slowing moving landslide in Nishiikawa area, Tokushima, Japan (hereinafter called Nishiikawa landslide). By inserting stainless steel rod (5 m long with a diameter of 20 mm) into a borehole and attaching the AE sensor to the end of the rod exposed on the ground, the acoustic emissions possibly resulting from the shear behavior of sandy materials that were set into the borehole were recorded.

As the third phase, we installed an inclinometer and a seismometer on Nishiikawa landslide. The inclinometer with a resolution of  $0.002^{\circ}/\text{mV}$  was inserted into the ground to a depth of about 2 m. Both the seismometer and inclinometer have been recorded continuously at a sampling frequency of 100 Hz. To further examine the creeping behavior of Nishiikawa landslide, we conducted model tests and examine the piston flow of ground water.

### **3. Summary of Research Findings**

The results of our laboratory tests suggested that during the granular shearing process there was a strong correlation between stick-slip events and the distribution of AE characteristics. We found that many different types of acoustic emissions are generated during particle shearing. The high-energy AE signals can accurately indicate structure failure. In addition, friction AE and local failure AE can represent the gradual damage process and can be used as important characteristic indicators for particle stability monitoring.

The AE monitoring system installed in Nishiikawa landslide did not allow us to conduct real time recording of the AE. We tried to get recordings onsite when we had field trips to this landslide, but every time the recording system just enabled us to get the recordings for a period of several minutes. Through analyzing the recorded data, we understood that we failed to get any AE recordings, probably because this landslide did not show any movement within our monitoring periods.

We obtained valuable data on the seismic response and landslide mass through the seismometer and inclinometer. These data enabled us to better understand the movement of the slowly moving landslide mass.

In this report, artificial rainfall experiments were carried out on cylindrical tubes filled with silica sand to investigate the process of piston flow. The results of our experiments show that the behavior of pore water pressure in the cylindrical pipe is related to the existence of pore air pressure sealed by the wetting front. Furthermore, this air pressure was affected by grain size, void ratio, and initial water content.

## **4. Details**

### **4.1 Laboratory Tests and Results**

To detect the precursors for the occurrence of landslides and then provide information for the landslide disaster mitigation, as the first phase, we conducted a series of direct shear-AE tests to investigate the relationship between characteristics of AE and mechanical behavior of granular in stick-slip events.

#### **4.1.1 Background**

Particles of different sizes and shapes are the basic components of rock and soil (Etienne, 2020). Through the interaction between the particles, a framework structure with load-bearing capacity is formed. Granular materials play a key role in the occurrence of geological disasters (Coulais et al., 2014; Kocharyan et al., 2014). For example, in a fault zone, there are a large number of broken rock particles. When the structure composed of particles become unstable, the blocks on both sides of the particles will be dislocated to form an earthquake (Lherminier et al., 2019; Ostapchuk et al., 2019). Similarly, other geological disasters such as landslides, soil liquefaction, and debris flow are also caused by self-organized critical behavior (Dalton and Corcoran, 2001; Michlmayr et al., 2017), frictional sliding (Wu et al., 2017), and dynamic behavior of particles (Doanh et al., 2017). So, studying the mechanical behavior of granular media, especially the stick-slip phenomenon (Kocharyan et al., 2017; Leeman et al., 2016; Scuderi et al., 2017) during shear process, will help us

understand the formation process of disasters and provide relevant theories for disaster forecasting and early warning (Hayman et al., 2011; Hedayat et al., 2014; Johnson et al., 2013; Kaproth and Marone, 2013).

However, for large-scale rock or soil, it is difficult to monitor the force and deformation of the internal structure in real time in practical applications. Scholars have noticed that deformation related to the interaction between particles is accompanied by the rapid release of elastic strain energy, stored between particles, in the form of elastic body waves (Lin et al., 2019; Ostapchuk et al., 2016; Smith and Dixon, 2019a). These elastic waves, known as acoustic emissions (AE) (Belov and Konstantinov, 1994; Deutsch et al., 1989; Kousteni et al., 1999; Lord and Koerner, 1975; Muravin et al., 1987; Zinovi, 2017), can be received by AE sensors mounted on the surface of the structure and converted into electrical signals. The current main research approach is to conduct mechanical and AE tests simultaneously during the particle shear process, and establish the relationships between AE parameters and mechanical behavior (Knuth et al., 2013; Lin et al., 2020; Xiao et al., 2019). So, in the field of stability monitoring of rock and soil, the AE signal can be related to the interior mechanics and deformation of geological materials. For this purpose, scholars have done many mechanical tests on model systems, in combination with AE measurements. These studies effectively provide a relationship between AE and the particle shear deformation process. For instance, Dixon (Dixon et al., 2018) used the quantitative relationship between the AE rate and sliding velocity to establish an early warning system (EWS) for landslides; Jiang (Jiang et al., 2017) found that the generation of AE preceded the changes in shear strength; and Smith (Smith and Dixon, 2019b) found the relationships between AE energy and boundary work. Since the AE of a granular material is generated by a variety of internal structural changes (Coulais et al., 2014), including friction, sliding, and crushing of particles (Johnson et al., 2013), there are many different types of AE during the shear process. Therefore, it is necessary to further research the AE produced by different sources. The AE parameters can then be classified to more accurately characterize the various states of the shear process and provide a basis for automatic (such as machine learning) monitoring and early warning (Deng et al., 2021; Hulbert et al., 2018; Ren et al., 2019). This type of research is relatively rare to date.

Here we explored the correlation between mechanical and AE behavior through a series of direct shear tests of granular materials under different loading conditions. We focus on finding the relationship between stick-slip and AE features, to classify the different AE signals. Furthermore, the different mechanical properties of the particles being sheared can be monitored from the AE features, which reflect the process of self-organization of the internal structure. The distribution of AE in the stick-slip process can be used to predict the structural failure of granular material.

#### 4.1.2 Methodology

In the direct shear test, we used a linear shear apparatus which can be set to different load speeds from 0.01 to 2.4 mm/min and normal stresses from 1 kPa to 1 MPa. We used spherical glass beads (1.0–1.5 mm diameter, glass density 2.50 g/cm<sup>3</sup>) to represent particles. Glass beads without water were dropped into the shear box which has a cylindrical specimen chamber with  $\Phi$  61.8 mm  $\times$  H 40 mm to produce a “loosely packed” specimen. The schematic of the test system is shown in Fig. 1. All specimens had the same density of 1.54 g/cm<sup>3</sup> and initial porosity of 0.38. Sixteen specimens were tested. Shearing was performed in a strain-controlled way at a constant shear speed of  $v_s = 0.1, 0.4, 0.8$  or 1.2 mm/min and

constant normal stress of  $\sigma_n = 50, 100, 200$  or  $300$  kPa. We measured shear stress ( $\tau$ ) and vertical displacement ( $s_n$ ) during the test using the force sensor and displacement transducer (LVDT), respectively. A summary of the direct shear tests performed is shown in Table 1.

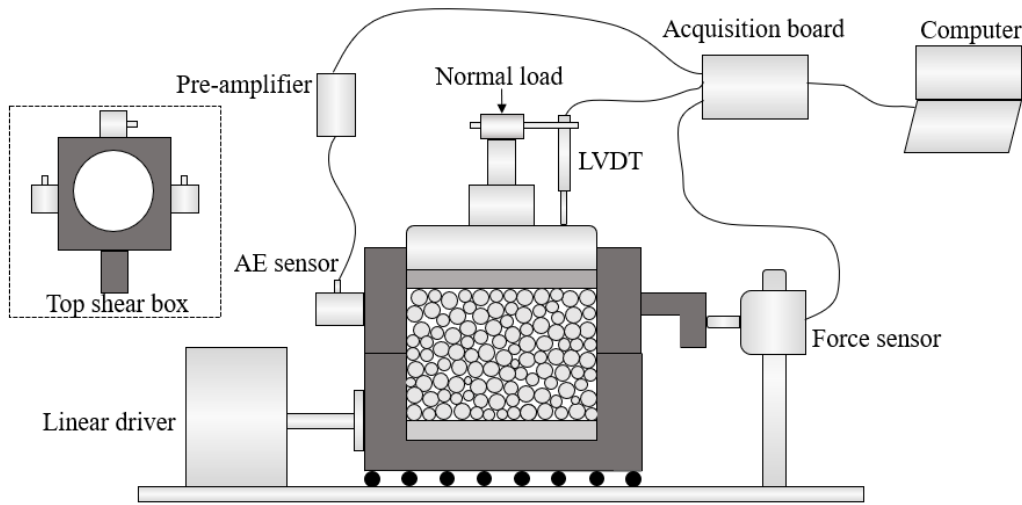


**Fig. 1** Schematic of the direct shear test with AE system

**Table 1** Summary of the direct shear tests performed in this study

| No. | Diameter (mm) | Load Speed (mm/min) | Normal Stress (kPa) | No. | Diameter (mm) | Load Speed (mm/min) | Normal Stress (kPa) |     |     |
|-----|---------------|---------------------|---------------------|-----|---------------|---------------------|---------------------|-----|-----|
| 1   | 1.0 -1.5      | 0.1                 | 50                  | 5   | 1.0 -1.5      | 0.4                 | 50                  |     |     |
| 2   |               |                     | 100                 | 6   |               |                     | 100                 |     |     |
| 3   |               |                     | 200                 | 7   |               |                     | 200                 |     |     |
| 4   |               |                     | 300                 | 8   |               |                     | 300                 |     |     |
| 9   |               | 0.8                 | 1.2                 | 50  |               | 13                  | 1.2                 | 1.2 | 50  |
| 10  |               |                     |                     | 100 |               | 14                  |                     |     | 100 |
| 11  |               |                     |                     | 200 |               | 15                  |                     |     | 200 |
| 12  |               |                     |                     | 300 |               | 16                  |                     |     | 300 |

We chose a PCI-2 AE system made by Physical Acoustics Corporation (PAC) to measure the AE signals during the test. Three separate AE sensors were installed at the right, left and back surfaces of the top shear box. The AE sensors used were MISTRAS R6a piezoelectric transducers, whose sensitive frequency range was from 1 to 100 kHz, and the resonant frequency was 60 kHz. Using the external parameter interface of the AE system, we collected the AE waveform,  $\tau$  and  $s_n$  at the same time, which allowed us to accurately explore the relationship between mechanical behavior and AE. All three AE sensors had the same settings: the pre-amplifier gain was 40 dB gain, the band-pass filter frequency range was 20–100 kHz, the threshold was 40 dB and the sampling rate was 1 MHz to record the full AE waveform.

Fig. 2 shows the schematic of AE waveform and features diagram. Before starting the AE test, it's necessary to define a threshold which was 40 dB in this study. When the signal amplitude ( $V$ ) exceeds the threshold, it is considered that an AE

event occurs. The start time is defined as  $T_1$ . When the signal remains below the threshold for longer than the terminate time which is defined before test, the AE event terminates. The end time is defined as  $T_2$ . The duration time ( $T$ ) is defined as the duration from  $T_1$  to  $T_2$ . The AE amplitude ( $a$ ) is the maximum (positive or negative) AE signal excursion during an AE event. AE counts ( $C$ ) is the number of oscillations that exceed the threshold. Each AE has an ID which is numbered according to the time sequence of occurrence. Some calculation AE features used in this study are shown as follows.

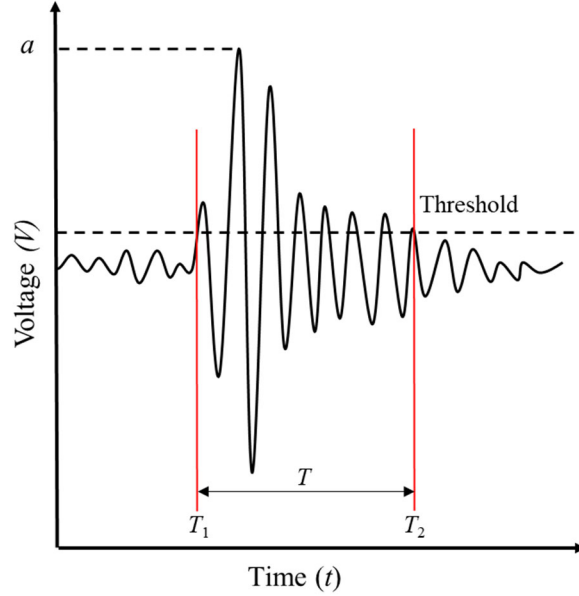


**Fig.2** Schematic of AE waveform and features (Zinovi, 2017)

(1). AE Energy ( $E$ ) (Zinovi, 2017) is the integral of the rectified voltage signal over the duration of the AE waveform.

It is represented by Eq. (1):

$$E = \int_{T_1}^{T_2} V(t) dt \quad (1)$$

$E$  represents the strength of elastic waves. The higher  $E$  is, the higher the level of the elastic stress wave would be.

(2). Average Frequency ( $f_a$ ) (Zinovi, 2017) is defined as AE counts ( $C$ ) divided by the duration time ( $T$ ).  $f_a$  can represent the frequency characteristics of the AE waveform.

(3). Root mean square ( $RMS$ ) (Zinovi, 2017) of the AE waveform is an electrical engineering power term defined as the rectified, time averaged AE signal, measured on a linear scale and reported in volts. It is represented by Eq. (2):

$$RMS = \sqrt{\frac{1}{T} \int_{T_1}^{T_2} (V(t))^2 dt} \quad (2)$$

$RMS$  reflects the power of the AE waveform; that is, for the same duration, a waveform with a larger  $RMS$  corresponds to a greater energy. Usually, a higher energy AE event corresponds to a larger  $RMS$ .

- (4). The concept of *b-value* (Liu et al., 2017; Riviere et al., 2018) was derived from seismology research to represent the earthquake magnitude. Researchers now also use *b-value* to describe the amplitude distribution of AE signals. It is given by Eq. (3):

$$\log[N(a)] = C - b \log(a) \quad (3)$$

Where  $a$  is the amplitude of AE;  $N$  is the number of AE with amplitude not less than  $a$ ; and  $C$  and  $b$  (the so-called *b-value*) are constants obtained by linear fitting. The greater the number of high-amplitude AEs, the smaller the *b-value*. There is a positive correlation between  $a$  and  $E$ , so *b-value* can easily describe the energy distribution in a single value. There have been many reports ( Ostapchuk et al., 2016; Riviere et al., 2018; Smith and Dixon, 2019a) on the application of *b-value* in AE monitoring of particulate materials.

- (5). We also defined  $N_{AE}$  as the cumulative number of AE;  $E_{AE}$  as the cumulative  $E$ ;  $K_N$  and  $K_E$  as the slopes of the  $N_{AE}$  and  $E_{AE}$  curves, respectively, during dilatancy; and  $R_{AE}$  as the occurrence rate of AE per every 0.005 mm shear displacement, also known as the AE rate in displacement domain.

### 4.1.3. Results

#### Typical mechanical and AE behavior during the whole shear process

Fig. 3 shows typical  $s - \tau$  curves with different normal stresses and shear speeds. The shear stress was mainly manifested as a corresponding “saw-tooth” periodicity, which built up gradually in a linear growth and then rapidly dropped. These cycles are caused by stick-slip behavior of granular materials (Johnson et al., 2013; Kocharyan et al., 2017; Leeman et al., 2016; Scuderi et al., 2017). Since the loading method of constant shear speed is used, the shear displacement is proportional to the loading time. So, the relatively long-time increase of shear stress is the “stick” event, and the rapid dropping of shear stress is the “slip” event. With increasing normal stress, Fig. 3(a), the stick-slip phenomenon becomes more obvious — the period of the stick-slip events increases, and the magnitude of the sudden drop in stress becomes larger. However, the change of shear speed has little effect on the  $s - \tau$  curves, and the period of stick-slip and the magnitude of the stress drop do not change noticeably (Fig.3(b)). As shown in Fig. 4,  $N_{AE}$  and  $E_{AE}$  are correlated positively with normal stress. It can be inferred that higher normal stress makes the contact between the particles closer and the interaction more intense, resulting in a greater number of AEs occurring during the shearing process. And, higher shear speed will reduce the time of interaction between particles. As a result, both  $N_{AE}$  and  $E_{AE}$  will show a decreasing trend when shear speed is faster.

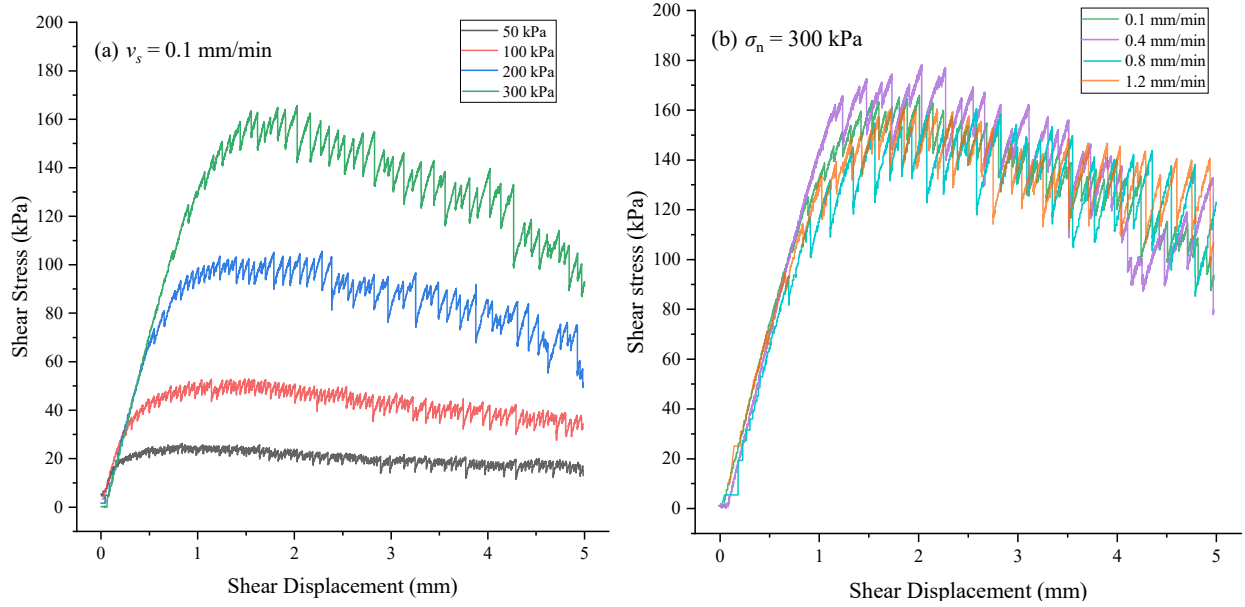


**Fig. 3** Typical shear displacement versus shear stress with different (a) normal stresses ( $v_s = 0.1$  mm/min) and (b) shear speeds ( $\sigma_n = 300$  kPa);

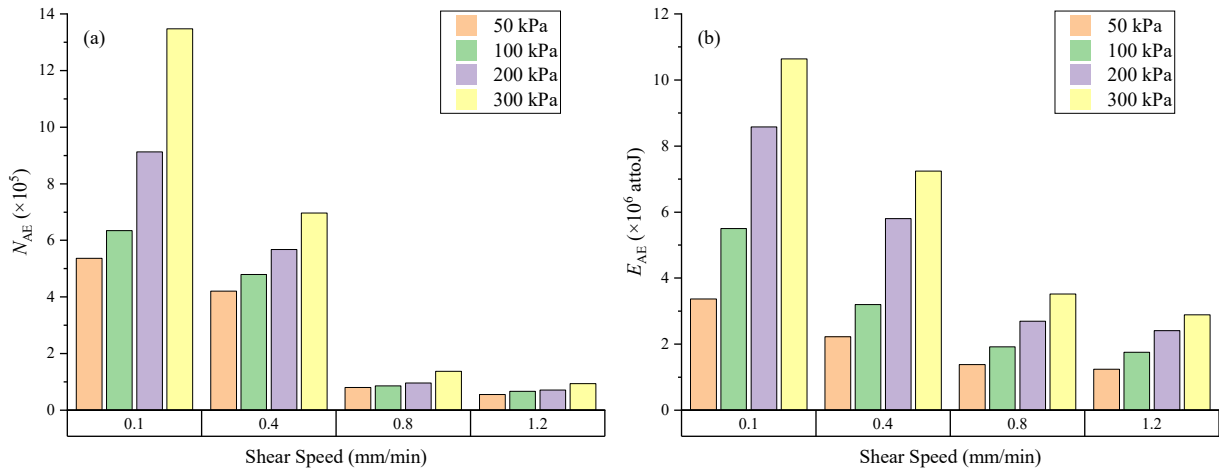


**Fig. 4** (a) Count of AE for different normal stresses and shear speeds; (b) cumulative AE energy for different shear speeds and normal stresses;

To investigate the relationship between mechanics and AE behavior, one representative result (from test No. 4) is illustrated in Fig. 5, which reveals the links between the mechanical ( $\tau$ ,  $s_n$ ) and AE ( $R_{AE}$ ,  $E$ ,  $N_{AE}$  and  $E_{AE}$ ) features of shearing sample. From Fig. 5 (a, b, c) we can find that the  $s_n$  decreased initially. That means the sample was compressed in the beginning time, while both  $R_{AE}$  and  $E$  were at a low level;  $N_{AE}$  and  $E_{AE}$  increased slowly. The minimum in  $s_n$  is where the porosity was the lowest. Then  $s_n$  began to increase, meaning that the sample began to dilate. It is worth noting that each slip event was accompanied by a large change in  $s_n$ , a rapid increase of  $R_{AE}$  and a high-energy AE which was monitored by three individual AE sensors. When  $s_n$  began to increase, the slopes of  $N_{AE}$  and  $E_{AE}$  became greater. Both showed a good linear correlation ( $K_N = 5.89E+6$ ,  $R^2 = 0.999$  and  $K_E = 2.13E+6$ ,  $R^2 = 0.997$ ).

Many AEs were detected in each test. The most (test No. 4) detected 134,622 AEs, and the least (test No. 13) detected 8,652 AEs. Fig. 6 shows the AE energy distribution for the entire shear process of test No.4. We can find that low-energy AEs accounts for the vast majority, and high-energy AEs only accounts for a small proportion. In this case, AE with energy less than 62 attoJ accounted for 90% of all AE events and were evenly distributed; 9% of AE events had energies of 62–1617 attoJ; only 1% of AE events had energy greater than 1617 attoJ. The maximum AE energy was 30219 attoJ.

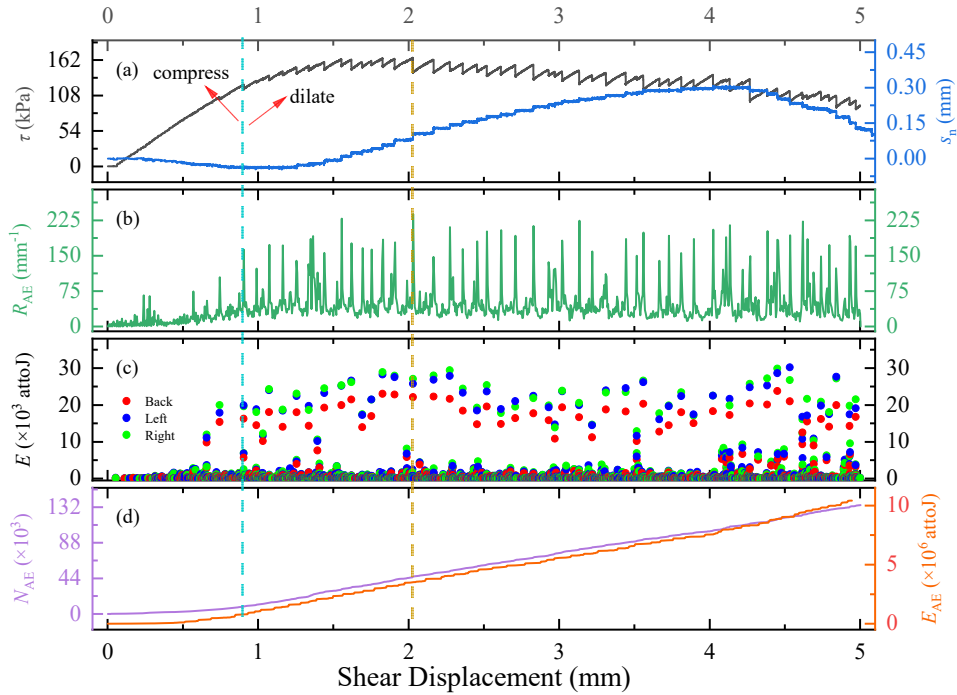


**Fig. 5** One representative result showing correlations between shear displacement and (a) shear stress ( $\tau$ ) and vertical displacement ( $s_n$ ), and (b) the occurrence rate of AE events within every 0.005 mm shearing displacement (AE rate,  $R_{AE}$ ); (c) AE energy ( $E$ ) scatter plots of three different AE sensors; and (d) the cumulative number of AE events ( $N_{AE}$ ) and cumulative AE energy ( $E_{AE}$ ).

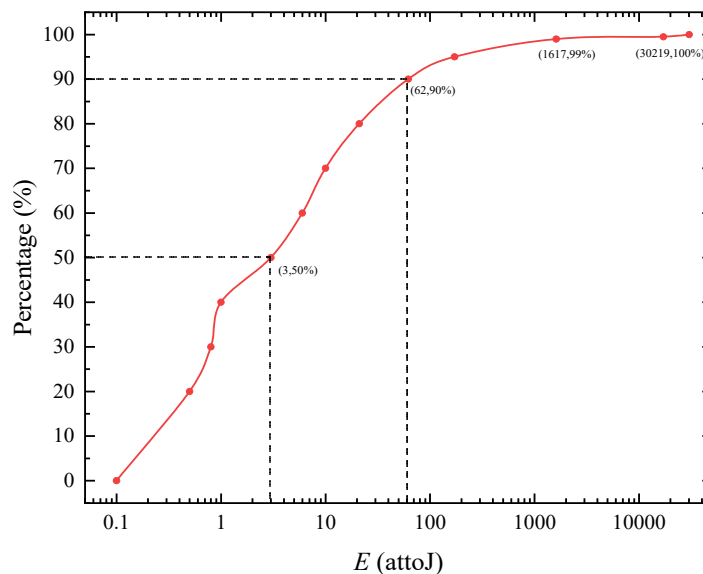


**Fig. 6** Overall AE energy distribution in the entire shear process of test No. 4

### AE features in stick-slip cycle

Stick-slip events are the main form in the particle shear process (Fig. 5 (a)). When the stick-slip event happened, the mechanical behavior and AE features changed in a cyclical way. So, it is worthwhile to use stick-slip as a research unit for in-depth analysis. In order to analyze the development process of stick-slip in detail, we divided one cycle into 11 stages (Fig. 7), s1 to s11, of which equally divided s1–s10 belong to the stick event and s11 represents the slip event. We define the stress drop as the change in shear stress from the maximum value in the slip event, denoted by  $\Delta\tau$ , and, we denote the load time in a stick-slip period as  $\Delta t$ .

Fig. 8 shows two typical stick-slip events and uses different colors to distinguish each stage. In this way, we can distinguish and statistically analyze the relationship between mechanics and AE behavior in different stages of stick-slip. In the direct shear test, since the particles are constrained by the shear box in the shear direction but not in the normal direction, the change in particle structure is mainly reflected by the normal displacement ( $s_n$ ). From Fig. 8(a) we note that in the stick event where the stress approximately increases linearly (elastic energy storage),  $s_n$  only fluctuated slightly, that means the sample volume fluctuates over a small range during the energy storage stage, in which the particle structure is relatively stable; however, in the slip event where the stress drops rapidly (energy release),  $s_n$  underwent a major change (either an increase or reduction), which means the sample has a large volume change, indicating that the particle structure has been reorganized, and the force chain between the particles was broken, releasing a large amount of elastic energy. This step-change behavior implies that drastic changes in the granular structure only occurred during the slip event.

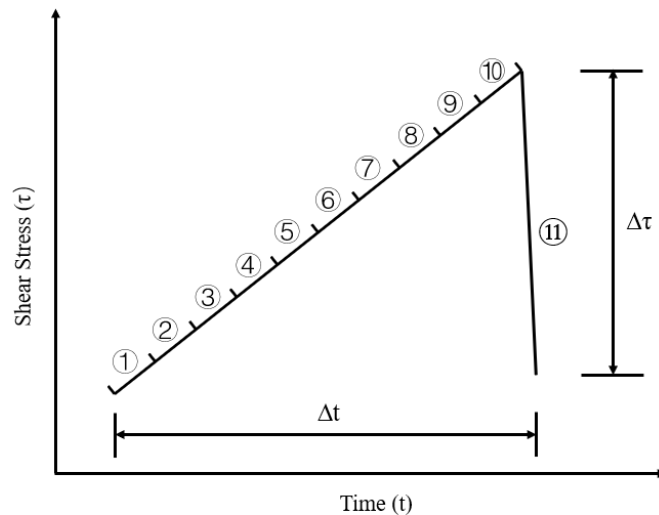
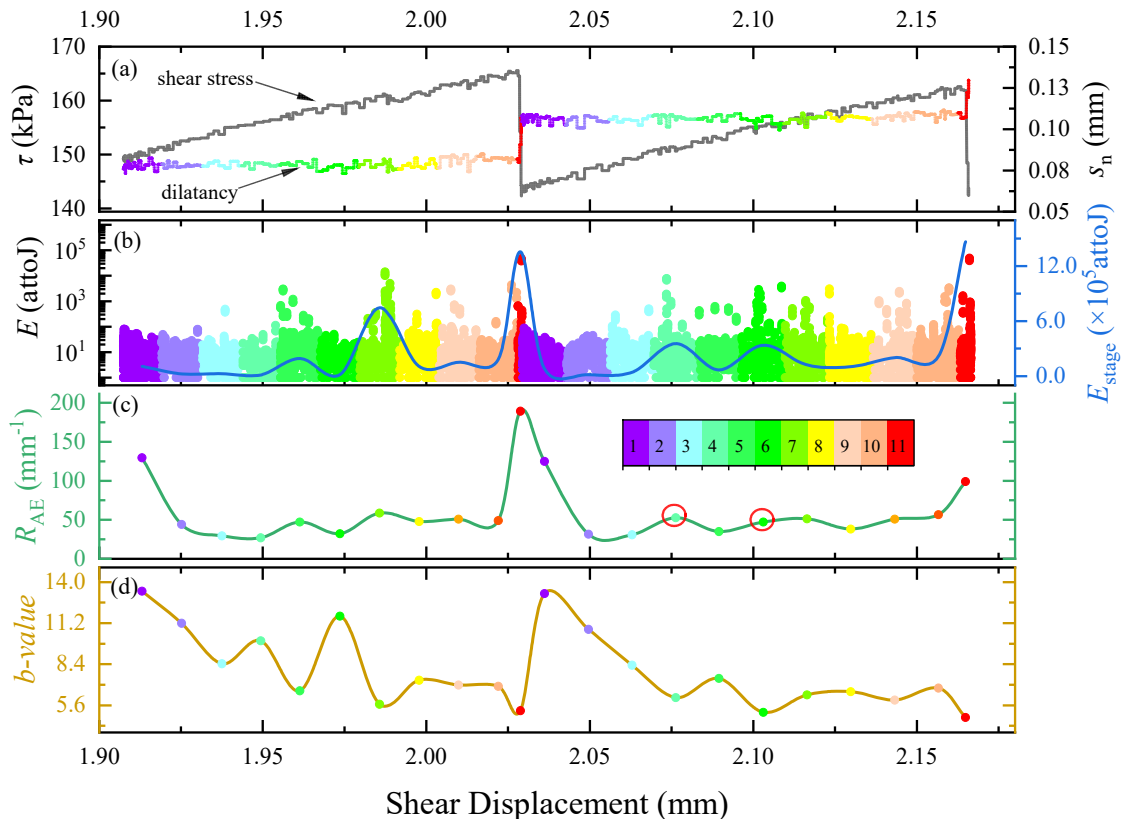


**Fig. 7** An illustration of stick-slip. The process can be divided into two parts: a linear increase in shear stress (which was divided into 10 stages of time). The second part is a rapid drop in stress, which occurs in stage 11.

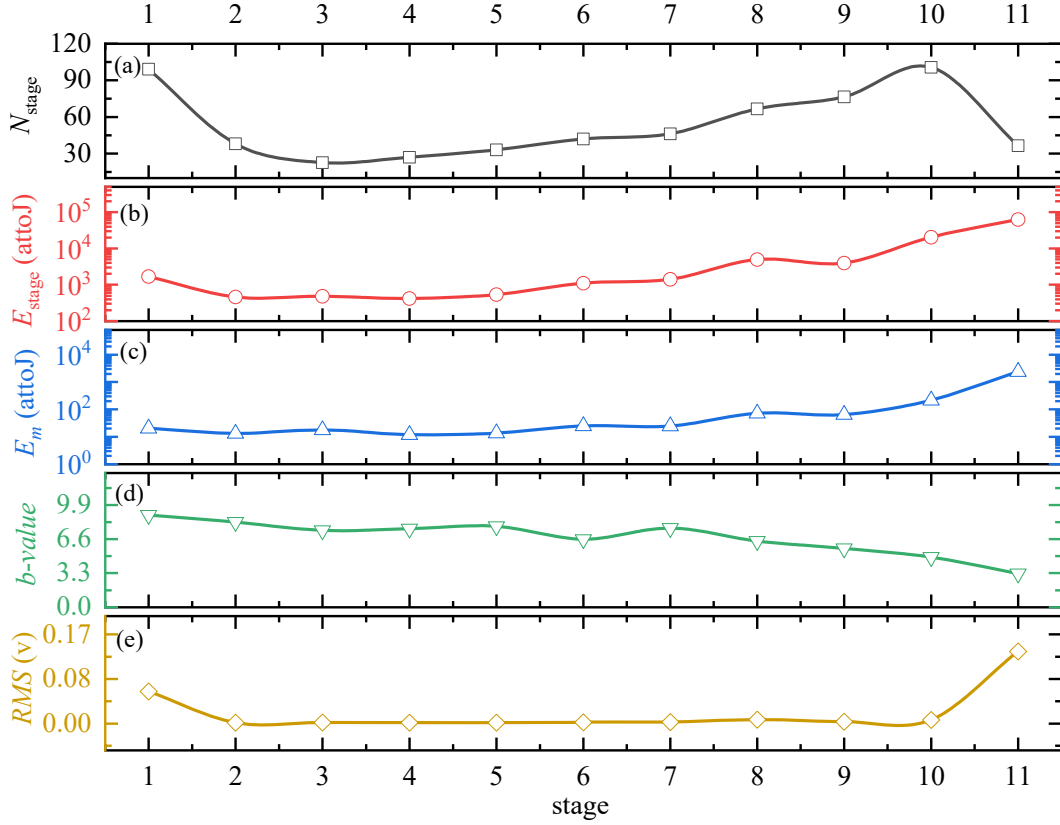
The energy scatter diagram in Fig. 8(b) shows that the energies in stages s1 and s2 are small; while those in s3–s10 are similar to those for s1 and s2 on the whole, although occasionally there are some AEs with energy greater than 100 attoJ. All of the AEs with very high energies happened in s11. The sums of the AE energies in each stage ( $E_{\text{stage}}$ ), are shown in Fig. 8(b); note that  $E_{\text{stage}}$  is small in the initial stages. As the shear stress increases,  $E_{\text{stage}}$  will fluctuate. In s11, the energy released by the sudden stress drop is much greater than that released by the other changes in stick event.

Fig. 8(c) shows  $R_{AE}$  in each stage. When a new cycle starts,  $R_{AE}$  is at a higher level, occasionally even higher than during the preceding s11. By the second stage,  $R_{AE}$  has returned to a low level. As the stress increases,  $R_{AE}$  gradually increases and fluctuates. When slip occurs,  $R_{AE}$  increases sharply.

We calculated the  $b$ -value for each stage as shown in Fig. 8(d). In each cycle, the  $b$ -value is the largest in s1, and then gradually decreases, reaching a minimum at s11. Compared with the curve in Fig. 8(b), the peak of the energy curve always corresponds to the trough of the  $b$ -value curve. As shown in Fig. 8(c), in s4 and s6 (marked with red circles), both  $E_{stage}$  and  $R_{AE}$  are only slightly different, but the  $b$ -value of s6 is noticeably less than the  $b$ -value of s4, which means that there are more AE events with higher energy in s6 than in s4. Thus the  $b$ -value can be used to effectively determine the energy distribution of the AEs (Liu et al., 2017; Riviere et al., 2018).



**Fig. 8** One representative result (two stick-slip cycles from test 4) showing correlations between (a) shear stress ( $\tau$ ) and vertical displacement ( $s_n$ ), and (b) AE energy ( $E$ ) scatter plots and the cumulative energy ( $E_{stage}$ ) in each stage; (c) AE rate ( $R_{AE}$ ), and (d) the  $b$ -value in each stage as a function of shear displacement.



**Fig. 9** Statistical averages (across all cycles of test 4) of AE parameters in each stage. (a) total number of AEs in each stage ( $N_{\text{stage}}$ ), (b)  $E_{\text{stage}}$ , (c) average  $E$  of each stage ( $E_m$ ), (d)  $b$ -value, (e)  $RMS$

Further, we counted the average of five AE features in each stage for all cycles (Fig. 9) to analyze their changes in stick-slip. At the beginning of a new cycle, there are more AEs (Fig. 9(a)); the number then quickly decreases before gradually increasing with increasing shear stress. Because the first ten stages are equally spaced,  $N_{\text{stage}}$  and  $R_{\text{AE}}$  are equivalent. However, in stage 11, although there are few AEs,  $R_{\text{AE}}$  is much higher than in the other stages, because of the instantaneous nature of the slip process (Fig. 7, Fig. 8(c)).

Fig. 9(a, b, c) shows that in s1–s6,  $E_m$  is low, and  $E_{\text{stage}}$  is mainly related to  $N_{\text{stage}}$ ;  $N_{\text{stage}}$ ,  $E_{\text{stage}}$ , and  $E_m$  in s7–s10 all show an increasing trend; in s11  $E_{\text{stage}}$  and  $E_m$  are much higher than in other stages, showing clear maximum. It can be seen from Fig. 9(d) that the  $b$ -value shows a gradual decrease over the entire cycle, indicating that, in a cycle, the distribution of AE energy gradually shifts to the high-energy region. S1 has the largest proportion of low-energy AEs, while, in s11, high-energy AEs accounted for the largest proportion. Therefore, as shown in Fig. 8(d), the  $b$ -value shows a strong change between the two cycles. Therefore, the lower the  $b$ -value reflects the violent vibration of the sample, that is, the more unstable the particle structure (Ostapchuk and Morozova, 2020). So, the stability of the structure can be predicted by the change trend of the  $b$ -value. It is worth noting that, in Fig. 9(c) and Fig. 9(e),  $E_m$  of s1 is similar to that of s2–s10; however, its  $RMS$  is much higher than that of other stages. This difference in  $RMS$  is explored further in Fig. 10.

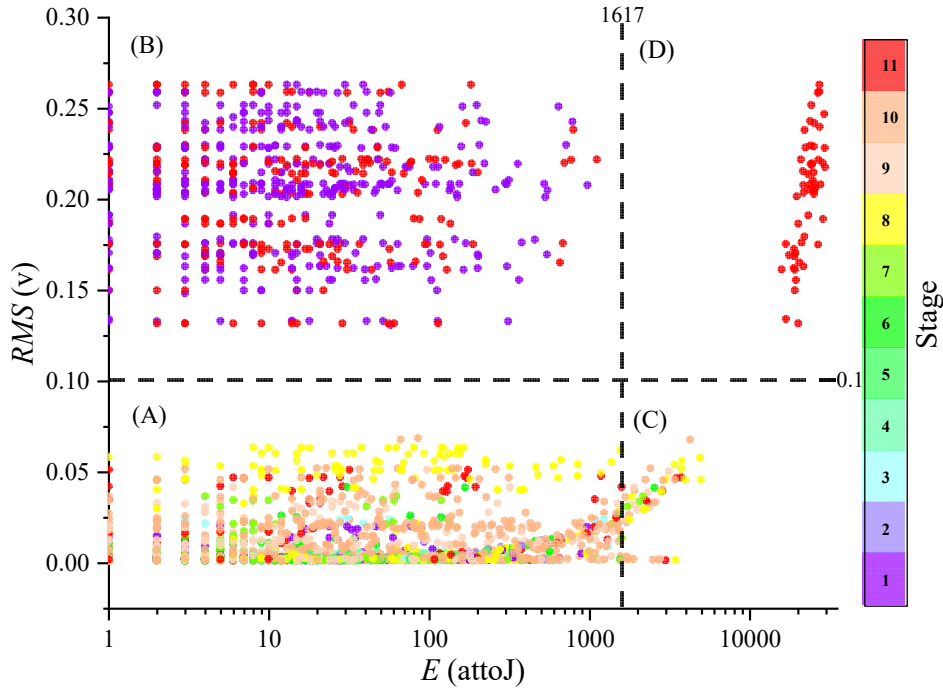


**Fig. 10** RMS- $E$  scatter plots of different stages of test 4

#### Four types of AE occur in stick-slip

Based on the different distribution of  $E$  and  $RMS$  in stick-slip events (Fig. 9), Fig. 10 gives a scatter plot of  $E$  and  $RMS$ , and uses different colors to distinguish the stages of the shear process. It can be seen from Fig. 10 that AEs were distributed in three different regions. According to the  $E$  distribution in Fig. 6, there is a significant change in the slope of the curve at  $E=1617$  attoJ. Therefore, using  $E=1617$  attoJ as the dividing line,  $E$  greater than 1617 attoJ is defined as the high-energy group accounting for 1%, and  $E$  less than 1617 attoJ is defined as the low-energy group accounting for 99%. In addition,  $RMS=0.1$  V was chosen as the dividing line of the RMS axis.  $RMS$  greater than 0.1 is defined as the high-RMS group, and others are defined as the low-RMS group. So, the E-RMS space is divided into 4 regions with  $E=1617$  attoJ and  $RMS=0.1$  V: in region A is the low-energy and low-RMS group; region B is the high-energy and low-RMS group; region C is the low-energy and high-RMS group; and region D is the high-energy and high-RMS group.

Fig. 11 gives the counts of AE in each stage individual the four regions. In region A, AEs occur in every stage. The number of AEs in this region is far more than the other three regions. So, the distribution shown for region A has a similar shape to the overall distribution shown in Fig. 9(a). In region B, AEs only occurred in s1 and s11. In fact, in periodic stick-slip events, s1 and s11 are continuous. That means these AEs should occur in continuous stages. In region C, AEs occurred from s6 and gradually increased in number, reaching a peak at s10; while in region D, AEs only occurred in s11. Furthermore, it can be seen from Fig. 12 that in each cycle, the AEs of region B are continuously generated after the region D signal occurs, and the AEs ID of both regions are continuous. So, AEs of region A must be generated after the end of region B. Combining Fig. 11 and 12, we can get the time sequence of the four regions AE in stick-slip event (Fig.13). In terms of time sequence, AEs in region A and C occur before region D, and AEs in region B occur after region

D; according to the distribution of AE, AEs in region A are a large number of continuous AE events, while the AE of region B, C, and D are a small number of burst AE events.

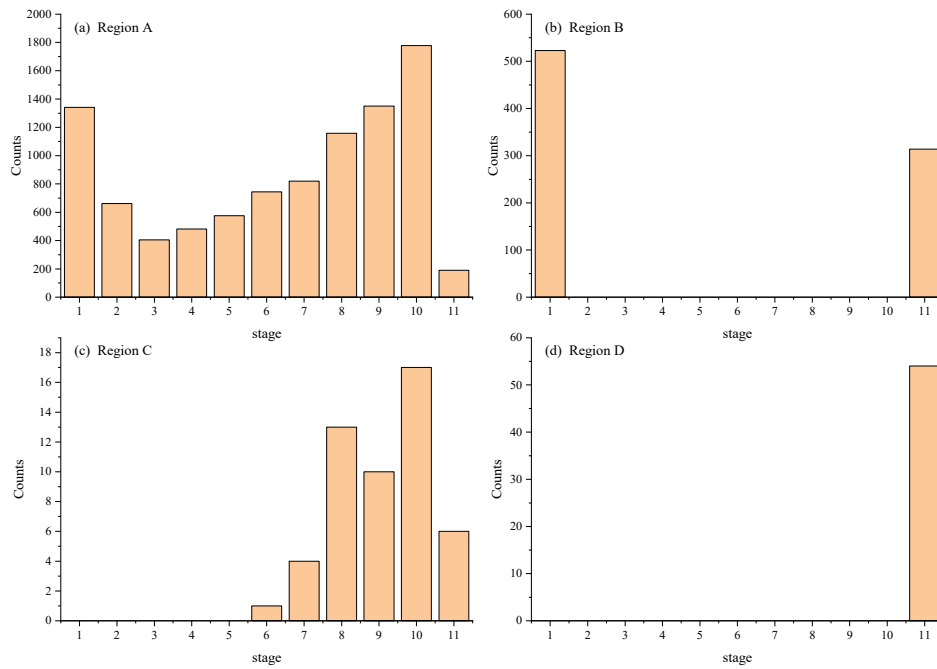


Fig. 11 Statistics on the numbers of AEs in different regions of Fig. 8

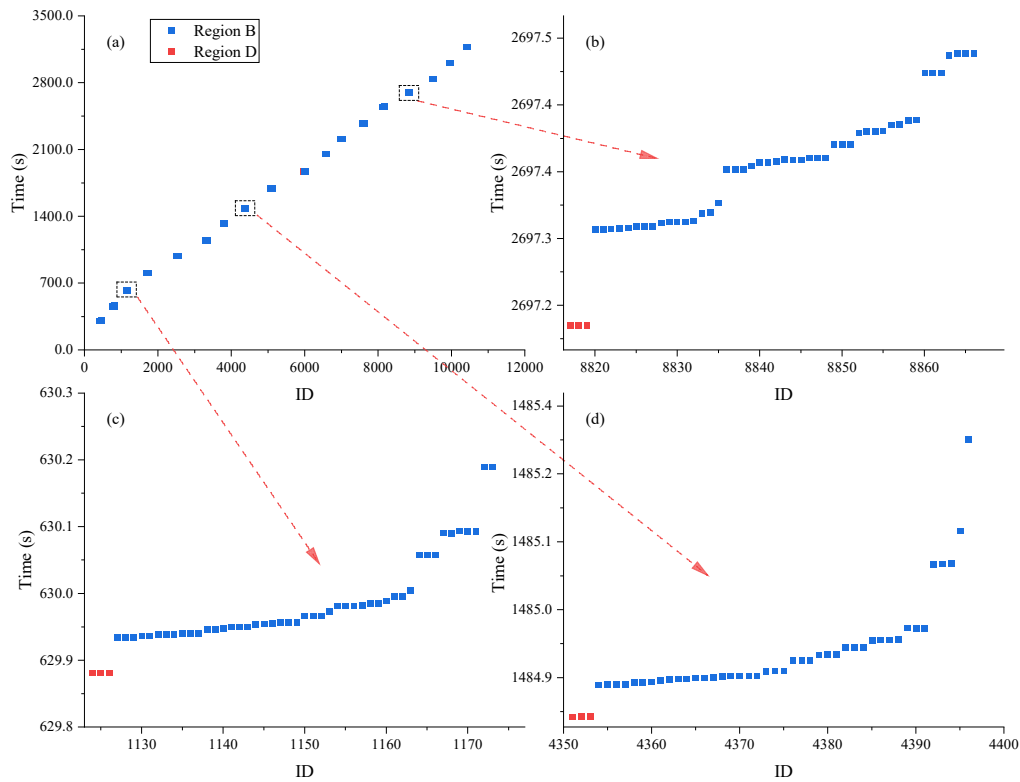
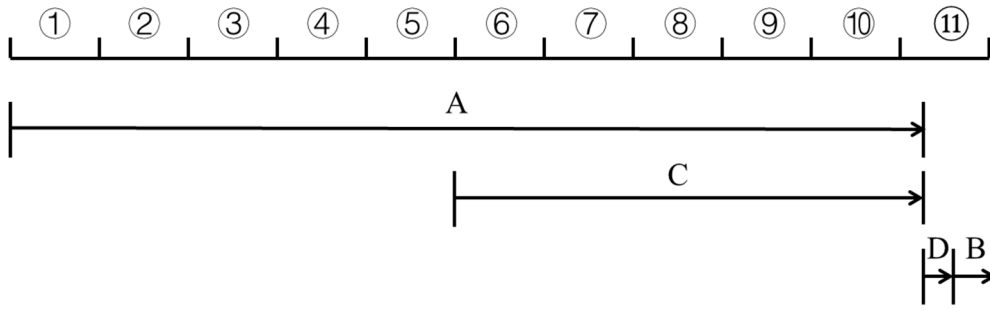
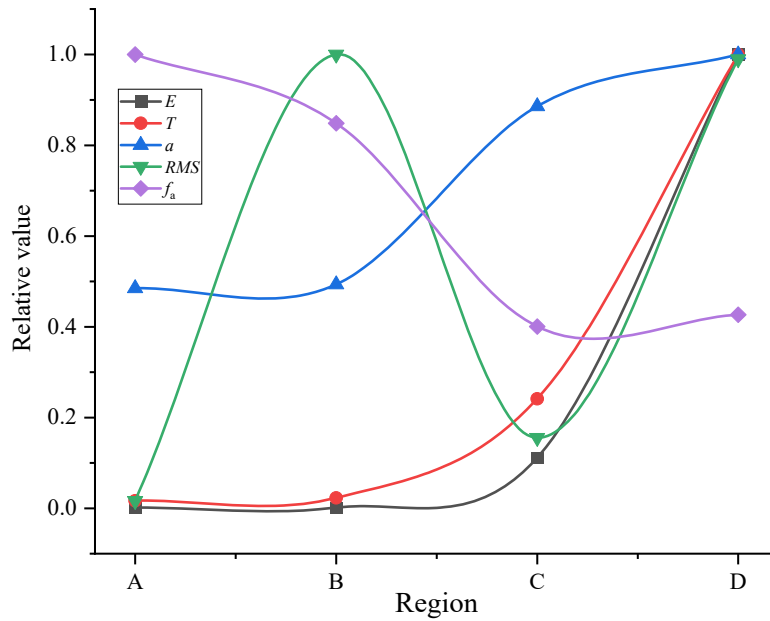


Fig. 12 (a) The sequence of AE occurrence in region B and D in all cycles. (b, c, d) a detailed diagram of one cycle.



**Fig. 13** The occurrence law of four regions AEs in stick-slip event.



**Fig. 14** Normalized value curves of five AE parameters in different regions of Fig. 10

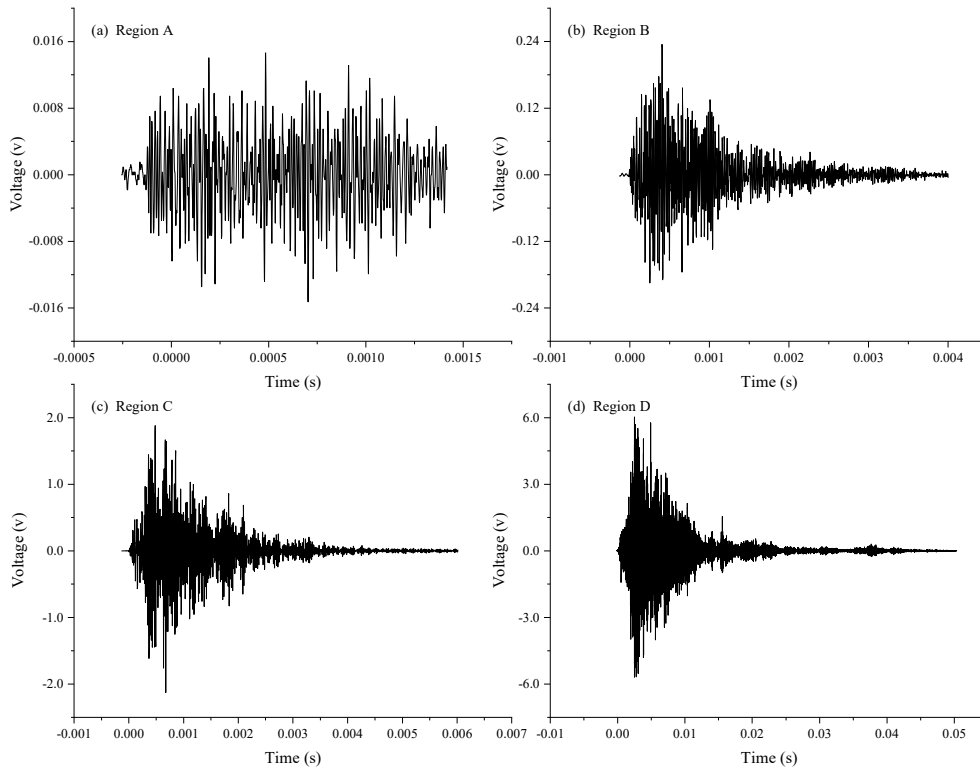


**Fig. 15** Typical AE waveforms from the four regions of Fig. 10

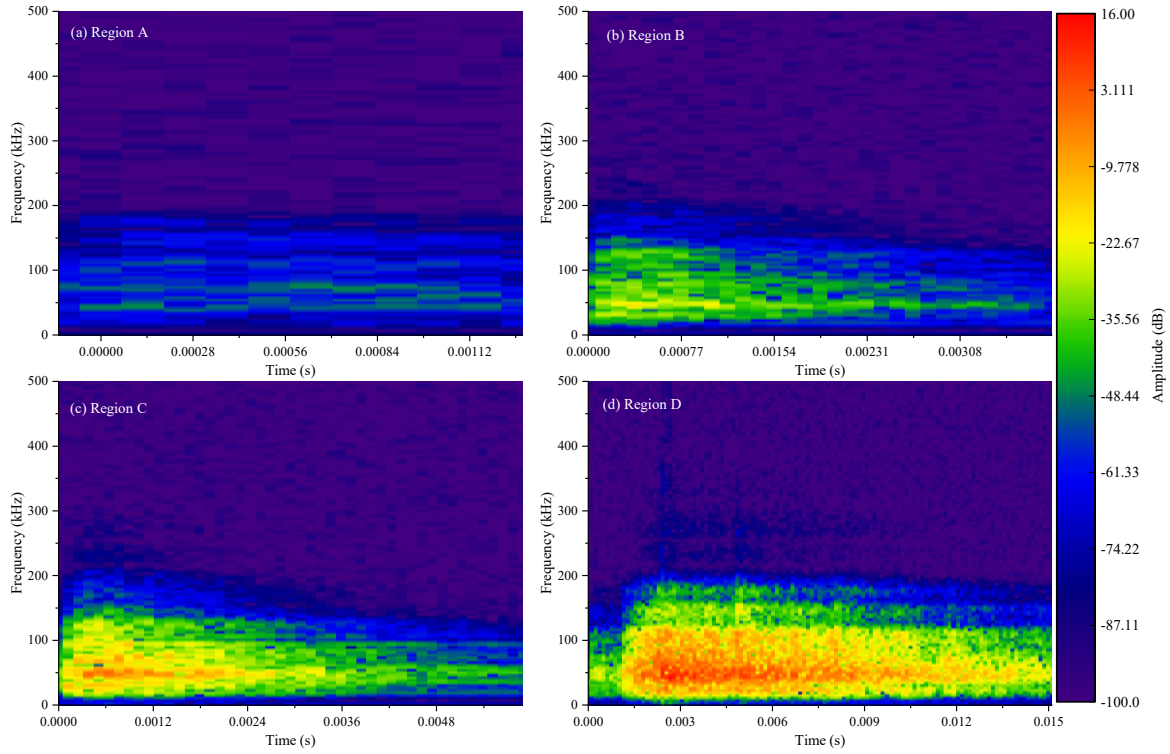


**Fig. 16** Time-frequency graphs of typical AE waveforms from the four regions of Fig. 10

**Table 2** The means of AE characteristic parameters in different regions of Fig. 10

| Region         | A       | B       | C        | D        |
|----------------|---------|---------|----------|----------|
| $E$ (attoJ)    | 32.79   | 35.39   | 2629.41  | 23661.89 |
| $T$ ( $\mu$ s) | 1016.24 | 1387.01 | 14607.59 | 60545.20 |
| $a$ (dB)       | 46.62   | 47.45   | 85.19    | 96.20    |
| $RMS$ (V)      | 0.0034  | 0.2047  | 0.0318   | 0.2026   |
| $f_a$ (kHz)    | 110.69  | 93.92   | 44.33    | 47.24    |

**Note:**  $E$  is energy,  $T$  is duration time,  $a$  is amplitude,  $RMS$  is root mean square of AE waveform, and  $f_a$  is average frequency

Then, we normalized values by their maximums to the range from 0 to 1, and they are shown in Fig. 14. From Table 2 and Fig. 14, we can see that the  $E$ ,  $T$ , and  $a$  of AE increase from A to D; conversely, the  $f_a$  of AE decreases. The  $RMS$  in regions B and D is considerably higher than it is in regions A and C. The AE signals of regions A and B are higher-frequency waveforms, while those of regions C and D are lower-frequency waveforms.

In the four regions, we select typical AE waveform whose parameters are similar to Table 2 and shown in Fig. 15. Fig. 16 present time-frequency maps of each typical waveform. The spectra in all four regions are concentrated below 200 kHz. The waveforms and spectral maps from region A have no significant peaks in the time domain, and the amplitude at each frequency is minimal. In contrast, the waveforms in regions B, C, and D show obvious steep rise and attenuation, and, high amplitude areas are mainly concentrated around 50 kHz, which is close to the resonance frequency of the AE sensor. In particular, the amplitude of region D is much higher than other regions.

#### 4.1.4. Discussion

After the trial, the glass beads were checked and found to be intact, indicating that no particles were broken during the shear process. It means that all the AEs were generated by the interaction between the particles (Jiang et al., 2017; Zhang et al., 2020). On the basis of a comprehensive analysis of Figs. 10–16, the distributions and waveform characteristics of the AE in the four regions of Fig. 10 can be classified into four types:

##### **Friction AE signal between particles — Region A**

It can be seen from Fig. 15(a) and Fig. 16(a) that the AE waveform in region A is stable with no significant fluctuations. The AEs of this region are low energy ( $E$ ), short duration ( $T$ ), low  $RMS$  and high average frequency ( $f_a$ ), with most AEs occurring during the stick event where energy was stored. As mentioned earlier, in stick event, there is no significant change in the particle structure, so the particles are mainly undergoing slight relative movements, from which it is concluded that this type of AE is a low-energy and short-time friction signal (Akella et al., 2018). AE signal produced by small local movements of particles and the movement of shear belt particles. Due to the large amount of particle contact in the specimen under these conditions, there is an extremely large number of such AE events, which explains why most AEs occur in region A.

Interestingly, as Fig. 9(a) shows, the AEs in s1 are higher, at which point the stress of the specimen is at the lowest level in the stick-slip cycle. Considering the significant volume change in the specimen at each stress drop, s1 is a relatively unstable state after the recombination of the particle structure. As a result, a large number of particles will re-establish contact (Gao et al., 2019; Hayman et al., 2011) in s1, squeezing and rubbing each other, resulting in a large number of low energy friction AE. When particles are relatively stable, friction decreases and the number of AEs produced decreases. Subsequently, with the increase of stress, the contact between particles is closer, the interaction between particles increases, and the number of AEs generated increases, as seen between s2 and s10. It can be concluded that the incidence of AEs in region A reflects the overall stability of the particle structure. The more unstable the structure is, the more significant the friction between particles will be, and the more AEs will be generated.

##### **High-energy AE signal caused by structural failure — Region D**

In region D, AEs only occur in the stress-drop process. The energies of these AEs events are much higher than those in other regions, and each stress drop is associated with a single AE event that is simultaneously detected by all three AE sensors distributed around the shear box (Fig.1). From this, it can be seen that region D represents high-energy AE events caused by the sudden release of elastic energy as the internal structure of the sample is reorganized (Michlmayr et al., 2013). When a slip event happens, the force chain of particle structure established in the stick event will be broken, and a new force chain will be established in a new cycle. AEs in this region are characterized by  $a$ ,  $E$ ,  $RMS$ , and  $T$  far greater than those in other regions, and relatively low  $f_a$ . These AEs in region D are the indicative signals of structural failure.

##### **High-frequency vibration AE signal caused by strong vibration — Region B**

In region B, AEs only occur in s1 and s11. These two stages are sequential (s1 follows s11). From Fig.12 we can clearly

see, in each cycle, the AEs in region B start about 0.05-0.1 s after the AEs in region D occurred, and continues to occur within time about 0.2-0.4 s. And, they have a high *RMS*, similar to that found in region D, while *T* is much shorter, *a* and *E* are low, and the high  $f_a$  is similar to that seen in region A. Although no relevant literature has been found to confirm the cause of this kind of AE, based on the time sequence and characteristics of its occurrence, we can infer these AEs which are high-frequency vibration signals caused by high-energy elastic waves released by the sudden stress drop. These AE signals represent the gradual dissipation of the high-energy elastic wave generated after the stress drops.

#### ***Intermediate-energy AE signal caused by local structure failure — Region C***

In region C, AEs are only found in s5–s11, and are less numerous. The AE waveforms in regions C and D exhibit similar bursts (Fig.15(c, d)) and low  $f_a$ , except that *a* and *E* are much smaller in region C than in region D. It can be concluded that those AEs that belong in region C are similar those from region D, in that they represent the sudden release of stress waves inside the specimen. So, the AE data points in region C and D conforms to the same distribution law. However, there is an obvious discontinuity region between C and D as shown in Fig. 10. This is because the change in shear stress in region D is much greater than that in region C. That means, the energy in region D is much higher than that in region C, so there is a large discontinuous region between C and D. Since the stress is not significantly reduced in the energy storage stage (Fig.8(a)), it is inferred that these stress waves are caused by local particle structure failure in the specimen.

In summary, the four different types of AE occur at different times in stick-slip events (Fig.13). The occurrence of AEs in region D indicates the overall failure of particle structure. The AEs of regions A and C occur before D, and the AEs of region B occur after D. Therefore, to predict the failure of particle structure, only the AEs of regions A and C can be used. For region A, due to the interaction between particles, AEs continuously occurred during the entire shear process. The greater the AE rate ( $R_{AE}$ ) represents, the more intense the interaction between particles, and thus the structure will be more unstable. So, when the  $R_{AE}$  increases, it means that the specimen is in a state of gradual instability. It can be used in a predictive way. And, for region C, AEs are formed by the local failure of the structure before the final failure, which is similar to the microseismic phenomena observed before an earthquake. Therefore, the appearance of an AE signal in region C can also be used as an indicator of impending structural failure.

#### **4.1.5 Summary**

In this study, a series of direct-shear tests on glass beads was carried out and AE signals were collected to monitor the shear process. In view of the periodic stick-slip phenomenon of granular materials in the shear process, each stick-slip event was divided into 11 stages, and the AEs were analyzed statistically. The main conclusions are:

The shearing process produces four main types of AE signals: a low-energy and high-frequency AE generated by friction between particles, which occurs throughout the shear process, is the major type; the second is higher energy and low-frequency AE generated by local failure in the specimen; the third is the highest energy and low-frequency AE generated by overall failure of the specimen; and, the last is low-energy, high-frequency and high-*RMS* vibration AE caused by the highest energy elastic wave.

Periodic stick-slip events are the main manifestation of particle shear. According to the shear stress change curve and the distributions of different AE energy events, stick-slip can be divided into four parts: (1) The unstable period after the reorganization of the particle structure. This is mainly manifested in the initial stage of stick-slip, where there are many unstable initial contacts, and a large number of friction AE events are generated; (2) The reorganized particle structure reaches a stable state. This process mainly occurs between the second and fourth stages, and is characterized by a minimum number of AE events, which are mostly low-energy friction AEs; (3) Energy accumulation and local instability. During the shear stress growth, the interaction between particles increases, resulting in increased friction AEs and local failure due to the uneven distribution of force chains within the particles. The increase trend of  $R_{AE}$  or the appearance of local failure AE can be used as precursor signals of impending structural failure; (4) Overall failure. The shear stress drops rapidly, releasing a large amount of elastic energy, the specimen undergoes a large body change, the internal particle structure is reorganized, and an AE event with much greater energy appears.

The *b-value* can indicate the intensity of vibration inside the specimen. Therefore, in the shear process, the change of the incidence of AE signal, the occurrence of medium-to-high energy AE events and the change of *b-value* can be used to predict sample instability and for stability analysis.

Higher normal stress makes the contact between particles closer, which increases the number and energy of AEs. Higher shear speed reduces the interaction time between particles and mainly reduces the number of particle friction AEs.

#### 4.1.6 References

- Akella, V.S., Bandi, M.M., Hentschel, H.G.E., et al., (2018) Force distributions in frictional granular media. *Phys Rev E* 98: 012905.
- Belov, V.Z., Konstantinov, L.K., (1994) Application of Acoustic-Emission for Monitoring the Quality of Glass Granules and Ceramic Samples. *Atom Energy* 77: 512-514.
- Coulais, C., Behringer, R.P., Dauchot, O., (2014) How the ideal jamming point illuminates the world of granular media. *Soft Matter* 10: 1519-1536.
- Dalton, F., Corcoran, D., (2001) Self-organized criticality in a sheared granular stick-slip system. *Phys Rev E Stat Nonlin Soft Matter Phys* 63: 061312.
- Deng, L., Smith, A., Dixon, N., et al., (2021) Automatic classification of landslide kinematics using acoustic emission measurements and machine learning. *Landslides* (2021).[\\_](#)
- Deutsch, W.L., Koerner, R.M., Lord, A.E., (1989) Determination of Prestress of Insitu Soils Using Acoustic Emissions. *Geotech Eng-Asce* 115: 228-245.
- Dixon, N., Smith, A., Flint, J.A., et al., (2018) An acoustic emission landslide early warning system for communities in low-income and middle-income countries. *Landslides* 15: 1631-1644.
- Doanh, T., Abdelmoula, N., Gribaa, L., et al., (2017) Dynamic instabilities under isotropic drained compression of idealized granular materials. *Acta Geotechnica* 12: 657-676.

- Etienne Guyon, J.-Y.D., Farhang Radjai, (2020) *Built on Sand The Science of Granular Materials*. Mit Press.
- Gao, K., Guyer, R., Rougier, E., et al., (2019) From Stress Chains to Acoustic Emission. *Phys Rev Lett* 123: 048003.
- Hayman, N.W., Ducloué, L., Foco, K.L., et al., (2011) Granular Controls on Periodicity of Stick-Slip Events: Kinematics and Force-Chains in an Experimental Fault. *Pure Appl Geophys* 168: 2239-2257.
- Kousteni, A., Hill, R., Dixon, N., et al., (1999) Acoustic emission technique for monitoring soil and rock slope instability. *Slope Stability Engineering*, Vols 1 & 2: 151-156
- Hedayat, A., Pyrak-Nolte, L.J., Bobet, A., (2014) Precursors to the shear failure of rock discontinuities. *Geophysical Research Letters* 41: 5467-5475.
- Hulbert, C., Rouet-Leduc, B., Johnson, P.A., et al., (2018) Similarity of fast and slow earthquakes illuminated by machine learning. *Nature Geoscience* 12: 69-74.
- Jiang, Y., Wang, G., Kamai, T., (2017) Acoustic emission signature of mechanical failure: Insights from ring-shear friction experiments on granular materials. *Geophysical Research Letters* 44: 2782-2791.
- Johnson, P.A., Ferdowsi, B., Kaproth, B.M., et al., (2013) Acoustic emission and microslip precursors to stick-slip failure in sheared granular material. *Geophysical Research Letters* 40: 5627-5631.
- Kaproth, B.M., Marone, C., (2013) Slow earthquakes, preseismic velocity changes, and the origin of slow frictional stick-slip. *Science* 341: 1229-1232.
- Knuth, M.W., Tobin, H.J., Marone, C., (2013) Evolution of ultrasonic velocity and dynamic elastic moduli with shear strain in granular layers. *Granul Matter* 15: 499-515.
- Kocharyan, G.G., Novikov, V.A., Ostapchuk, A.A., et al., (2017) A study of different fault slip modes governed by the gouge material composition in laboratory experiments. *Geophys J Int* 208: 521-528.
- Kocharyan, G.G., Ostapchuk, A.A., Markov, V.K., et al., (2014) Some questions of geomechanics of the faults in the continental crust. *Izvestiya, Physics of the Solid Earth* 50: 355-366.
- Leeman, J.R., Saffer, D.M., Scuderi, M.M., et al., (2016) Laboratory observations of slow earthquakes and the spectrum of tectonic fault slip modes. *Nat Commun* 7: 11104.
- Lherminier, S., Planet, R., Vehel, V.L.D., et al., (2019) Continuously Sheared Granular Matter Reproduces in Detail Seismicity Laws. *Phys Rev Lett* 122: 218501.
- Lin, W., Liu, A., Mao, W., (2019) Use of acoustic emission to evaluate the micro-mechanical behavior of sands in single particle compression tests. *Ultrasonics* 99: 105962.
- Lin, W., Liu, A., Mao, W., et al., (2020) Acoustic emission behavior of granular soils with various ground conditions in drained triaxial compression tests. *Soils Found* 60: 929-943.
- Lord, A.E., Koerner, R.M., (1975) Acoustic Emissions in Soils and Their Use in Assessing Earth Dam Stability. *J Acoust Soc Am* 57: 516-519.
- Liu, X., Pan, M., Li, X., et al., (2017) B-Value Characteristics of Rock Acoustic Emission Under Impact Loading. *Springer Proc Phys* 179: 135-144.
- Michlmayr, G., Chalari, A., Clarke, A., et al., (2017) Fiber-optic high-resolution acoustic emission (AE) monitoring of slope failure. *Landslides* 14: 1139-1146.
- Michlmayr, G., Cohen, D., Or, D., (2013) Shear-induced force fluctuations and acoustic emissions in granular material.

- J Geophys Res-Sol Ea 118: 6086-6098.
- Muravin, G.B., Erminson, A.L., Sigalovskii, M.N., (1987) System for the Acoustic-Emission Investigation of Soil Movement. *Sov J Nondestr Test+* 23: 201-205
- Ostapchuk, A.A., Morozova, K.G., (2020) On the Mechanism of Laboratory Earthquake Nucleation Highlighted by Acoustic Emission. *Sci Rep-Uk* 10: 7245.
- Ostapchuk, A.A., Pavlov, D.V., Markov, V.K., et al., (2016) Study of acoustic emission signals during fracture shear deformation. *Acoust Phys+* 62: 505-513.
- Ostapchuk, A.A., Pavlov, D.V., Ruzhich, V.V., et al., (2019) Seismic-Acoustics of a Block Sliding Along a Fault. *Pure Appl Geophys* 177: 2641-2651.
- Ren, C.X., Dorostkar, O., Rouet-Leduc, B., et al., (2019) Machine Learning Reveals the State of Intermittent Frictional Dynamics in a Sheared Granular Fault. *Geophysical Research Letters* 46: 7395-7403.
- Riviere, J., Lv, Z., Johnson, P.A., et al., (2018) Evolution of b-value during the seismic cycle: Insights from laboratory experiments on simulated faults. *Earth Planet Sc Lett* 482: 407-413.
- Scuderi, M.M., Collettini, C., Viti, C., et al., (2017) Evolution of shear fabric in granular fault gouge from stable sliding to stick slip and implications for fault slip mode. *Geology*.
- Smith, A., Dixon, N., (2019a) Acoustic emission behaviour of dense sands. *Geotechnique* 69: 1107-1122.
- Smith, A., Dixon, N., (2019b) Acoustic emission generated by glass beads in compression and shearing. *Granul Matter* 21.
- Wu, K., Abriak, N., Becquart, F., et al., (2017) Shear mechanical behavior of model materials samples by experimental triaxial tests: case study of 4 mm diameter glass beads. *Granul Matter* 19.
- Xiao, Y., Wang, L., Jiang, X., et al., (2019) Acoustic Emission and Force Drop in Grain Crushing of Carbonate Sands. *Journal of Geotechnical and Geoenvironmental Engineering* 145.
- Zhang, G.K., Li, H.B., Wang, M.Y., et al., (2020) Crack initiation of granite under uniaxial compression tests: A comparison study. *J Rock Mech Geotech* 12: 656-666.
- Zinoviy Nazarchuk, V.S., Oleh Serhiyenko (2017) *Acoustic Emission Methodology and Application*. Springer.

## 4.2 Field monitoring

As the second phase of this study, we installed AE monitoring system in a slowly moving landslide in Nishi-Ikawa area (hereinafter called Nishi-Ikawa landslide), Tokushima, Japan. The landslide area consists mainly of green schist and partially of polytic schist. Figure 17 present the location of the study area and Figure 18 the plan of this landslide. This landslide was triggered by the cutting on the lower part of the slope in old landslide mass for the construction of a factory in 1973. Since then, to clarify the initiation and movement mechanisms of this landslide, detailed study had been conducted through drillings and different types of monitoring (Suemine et al, 1980; Suemine, 2004; Araiba and Suemine 1995; Furuya et al, 2013, among others). The veins of groundwater flow had also been examined by the results of 1-m-depth ground temperature survey (Fig. 18) in recent years, and more detailed topographic feature had been examined through LiDAR survey (Fig. 19) (Doshida et al., ).



Fig. 17. Location of the Nishi-Ikawa landslide (after Araiba and Suemine, 1998).

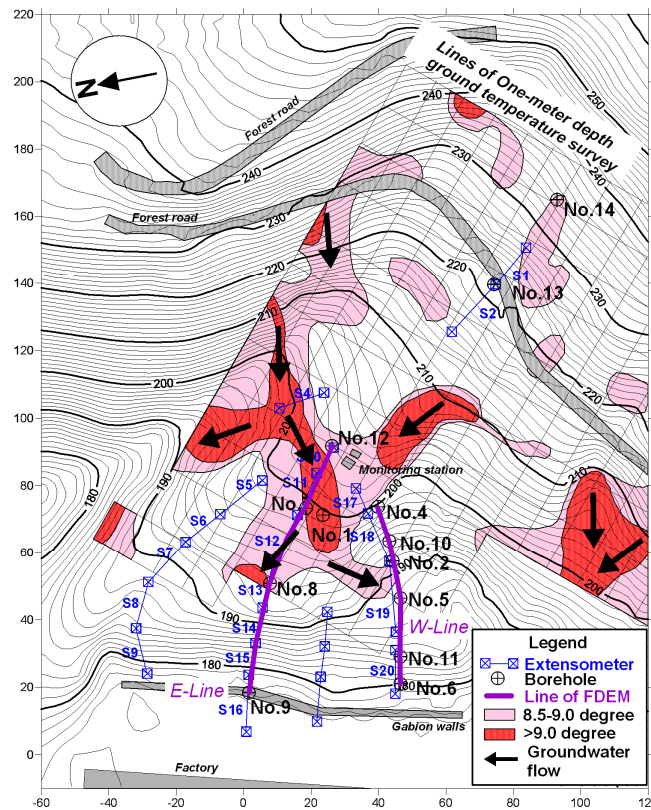
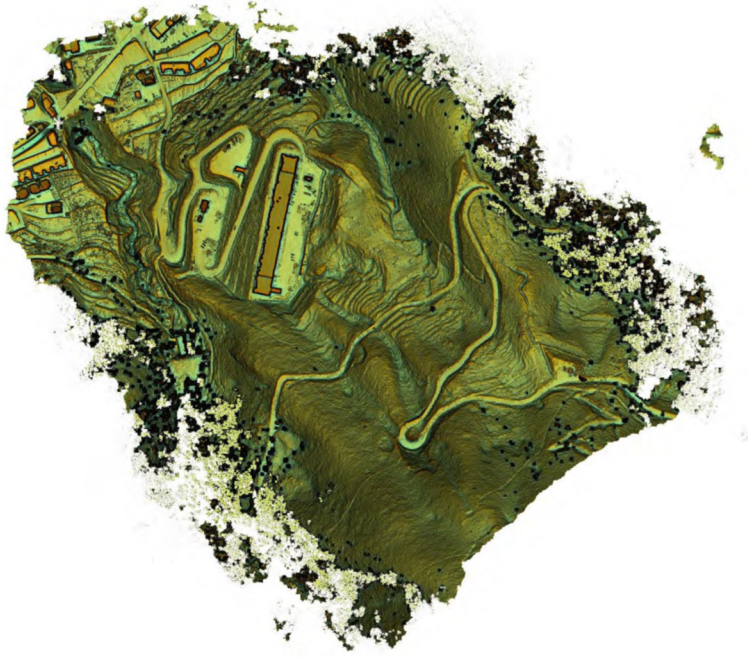
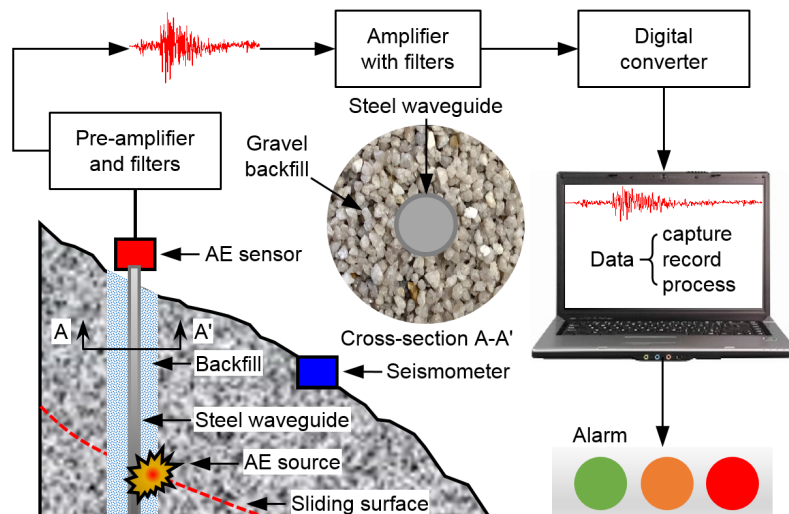


Fig. 18. Plan of Nishi-Ikawa landslide area



**Fig. 19.** Orthophoto of Nishi-Ikawa area (courtesy of Dr. Doshida Shoji at National Research Institute of Fire and Disaster, Japan)

To catch the possible AE signals, we inserted stainless steel rod (5 m long with a diameter of 20 mm) into a borehole and fulfilled the space between the steel rod and boring pipe by sand. We attached an AE sensor to the end of the rod exposed on the ground, and then recorded the signals from the AE sensor. Fig. 20 gives a schematic illustration of the monitoring system. It is noted that we planned to make continuous monitoring, but due to the limitation in the budget, we used a datalogger that was bought before for the laboratory experimental work in Disaster Prevention Research Institute, Kyoto University, and made short time monitoring every time when we had the field trip in Nishi-Ikawa landslide area. Unfortunately, we failed to distinguish any AE signals from the recorded limited data. Nevertheless, we bought a AE datalogger and will install it in the monitoring system to conduct continuous monitoring. We hope that we can report the data and results in future with progress of the monitoring.



**Fig.20.** Schematic image of the field monitoring system including AE sensor and seismometer.

As the third phase, we installed an inclinometer and a seismometer on Nishi-Ikawa landslide in March, 2023, inclinometer with a resolution of 0.002°/mV was inserted into the ground to a depth of about 2 m. Both the seismometer and inclinometer have been recorded continuously at a sampling frequency of 100 Hz. Therefore, we obtained a huge amount of data. Now detailed analysis on these data are on going, and we hope to be able to report the data soon. Further, to examine the creeping behavior of Nishi-Ikawa landslide, we conducted model tests and examine the piston flow of ground water, and the results had been reported in 古谷 他(2023).

## 5. Publications of Research Findings

LIU Ziming, JIANG Yao, WANG Daojie, FU Yanju (2022): Four types of acoustic emission characteristics during granular stick-slip Evolution. *J. Mt. Sci.* 19(1): 276-288.

Yao JIANG, Ziming Liu, Gonghui WANG (2023): Different Acoustic Emissions Source from the Evolution of Granular Stick-slip Events. 2022年京都大学防災研究所研究発表会, D203

古谷 元・幅下大地・Thanda WIN・王 功輝・末峯 章 (2023): 地下水の押し出し流に関するモデル実験. 2022年京都大学防災研究所研究発表会, D208

Shengshan WU, Gonghui WANG (2023): The Effect of Particle Shape on the Shear Behavior: Results of Tests on Rice Particles and Implication for High-mobility of Rock Avalanche. 2022年京都大学防災研究所研究発表会, D201

Bingcheng LIU, Shengshan WU, Gonghui WANG (2023): Development of Micro-fractures within Shear Zone Revealed by X-ray Micro-CT Scan: Examples from Rock Halite in Ring-shear Experiments. 2022年京都大学防災研究所研究発表会, D202

## 6. Other contributors to this Research

Gen Furuya, Professor, Toyama Prefectural University

Gonghui Wang, Professor, DPRI, Kyoto University

Issei Doi, Assistant Professor, DPRI, Kyoto University

Bingcheng Liu, Graduate School of Science, Kyoto University

Chao Huang, Graduate School of Science, Kyoto University

Shengshan Wu, Graduate School of Science, Kyoto University

### Note:

Finally, it is noted that this report is mainly based on the publications mentioned above. The contents of Section 3.2 are from the draft submitted for possible publication. A more detailed analysis of the results obtained by the study presented in Sections 3.1 and 3.3 is undergoing, and the results will be summarized in papers for possible publication in international journals in near future. We will make reports once these papers had been accepted for publication.